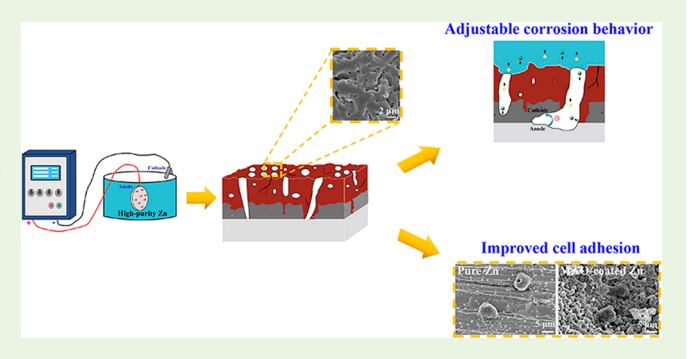


Formation Mechanism, Corrosion Behavior, and Cytocompatibility of Microarc Oxidation Coating on Absorbable High-Purity Zinc

Wei Yuan, † Bo Li, † Dafu Chen, *, § Donghui Zhu, lo Yong Han, *, † and Yufeng Zheng *, †, Lo

ABSTRACT: Microarc oxidation (MAO) has been regarded as one of the most effective techniques to suspend the corrosion rate of Mg-based alloys. In this research, MAO coating was successfully constructed on the surface of highpurity Zn for biomedical purpose. The microstructure, composition, corrosion behavior, and biocompatibility of MAO-coated samples were investigated. It was found that micro/nano pores were homogeneously distributed on the surface after MAO treatment in the electrolyte containing calcium and phosphorus components with pore size ranging from submicron scale to several micrometers. The MAO coating can modulate the corrosion behavior of pure Zn



substrate by means of chemical dissolution and galvanic corrosion between coating and substrate. MG63 cells cultured in the 100% extracts of MAO-coated sample exhibited significant cytotoxicity due to stimulated cell apoptosis induced by high concentration of released Zn²⁺, whereas excellent cytocompatibility was observed for 20% extracts. Meanwhile, cell adhesion was promoted on the porous structure generated during MAO process. These results suggested MAO treatment can achieve an accelerated corrosion adjustment, as well as a better cell adhesion on pure Zn.

KEYWORDS: high-purity zinc, microarc oxidation, degradation, biocompatibility

1. INTRODUCTION

Recently, much attention had been focused on zinc (Zn) as a new generation of biodegradable metal. Zn has always been selected as alloying elements in Mg and demonstrated beneficial effects on the corrosion resistance of Mg. 1,2 Because of the intermediate standard corrosion potential between that of Fe and Mg, Zn can be proposed as a promising alternative with preferable degradation rate to clinical requisites.³ Apart from the compromised corrosion behavior, the significant physiochemical properties also endow Zn with increasing interest. Zn is an essential metal element for humans and participates in many crucial physiological functions.⁴. It is proven that Zn has a stimulating effect on bone growth and mineralization.⁵ Zn interacts with vital hormones associated with bone formation, including testosterone, the thyroid hormones, insulin et al.6 In addition, Zn can also inhibit the osteoclastic bone resorption selectively and potently, accompanied by obvious inhibitory effect at the concentration as low as 10⁻¹⁴ M.⁵ In the past few years, a diversity of Zn-based materials has been developed for biomedical application, such as Zn-Mg,⁷ Zn-Ca,⁸ Zn-Sr,⁸ and Zn-Li⁹ alloy. Drelich et al. 10 implanted pure Zn wires into the abdominal aorta of Sprague-Dawley rat for 20 months and found a beneficial implant biointegration and safe degradation with excellent biocompatibility. Nonetheless, the corrosion rate of pure Zn in orthopedic environment is reported to be too slow considering the recovery process of injured tissue. Kafri et al. 11 added Fe into pure Zn as an alloying element to accelerate the corrosion rate of pure Zn by means of microgalvanic effect. Yang et al. 12 prepared zinc-hydroxyapatite composites and achieved an stepped-up corrosion behavior and improved osteogenesis. Meanwhile, an unsatisfactory bonding between pure Zn implant and bone was observed after 8 weeks' implantation.¹² Hence, the development of Zn-based materials with adjustable corrosion behavior and better osteointegration is eagerly anticipated.

Microarc oxidation (MAO) has been applied to in situ produce ceramic-like films on the surface of lightweight metals,

Received: September 18, 2018 Accepted: December 18, 2018 Published: December 18, 2018

Department of Materials Science and Engineering, College of Engineering, Peking University, Beijing 100871, China

[‡]State Key Laboratory for Mechanical Behavior of Materials, Xi'an Jiaotong University, Xi'an 710049, China

SLaboratory of Bone Tissue Engineering, Beijing Research Institute of Traumatology and Orthopaedics, Beijing JiShuiTan Hospital, Beijing 100035, China

Department of Biomedical Engineering, College of Engineering, University of North Texas, Denton, Texas 76207, United States $^\perp$ International Research Organization for Advanced Science and Technology, Kumamoto University, 2-39-1 Kurokami, Chuo-Ku, Kumamoto 860-8555, Japan

such as aluminum, 13 titanium, 14 magnesium, 15 and zirconium.¹⁶ MAO coatings are formed under high-voltage and composed of species derived from the electrolyte and substrate in proportions on the basis of discharge condition. 17,18 Furthermore, MAO treatment can also incorporate Ca and P ions into the coating by adjusting the constituents and concentration of the electrolyte. 19,20 Calcium phosphate is commonly proposed as a coating material on the surface of metallic materials for the sake of the fast fixation and excellent osteointegration in consideration of its bioactivity and osteoconductivity. 21,22 Some previous works have uncovered that MAO treatment was beneficial to corrosion resistance of Mg alloy with better fracture stabilization and bone-implant connections in the initial stage of implantation. Thereafter, a faster corrosion happened. ^{23,24} 3D printed porous Ti₆Al₄V has been proven to possess enhanced osteointegration by means of improved bone in-growth and interlocking between bone and implant after MAO treatment.²³ Whereas limited reports on MÃO of Zn were targeted at industrial applications, ^{25,26} none of them were associated with its influence on the corrosion of Zn in physiological environment and even the further biomedical applications. Rocca et al.²⁶ illustrated the process of the formation of "ceramic-like" coating during MAO treatment on Zn in KOH-based media. Stojadinović et al.²⁵ prepared MAO coating on Zn foil and investigated the structural and optical properties of the coating. The purpose of the present work is to prepare MAO porous coating containing calcium phosphate component on the surface of high-purity Zn and compare the corrosion behavior and biocompatibility of Zn with and without MAO treatment.

2. MATERIALS AND METHODS

2.1. Sample Preparation. The high-purity Zn (99.999%) ingot was purchased from Huludao Zinc Industry Co. China, Subsequently, the ingot underwent hot extrusion at $100\,^{\circ}\text{C}$ with an extrusion ration of 16-1. Afterward, the as-extruded rod was cut into disc samples with a size of $10\,\text{mm}$ in diameter and $2\,\text{mm}$ in thickness. Prior to studies, all samples were mechanically abraded with SiC paper in successive from $800\,$ to $2000\,$ grit, which were then ultrasonically cleaned in acetone, anhydrous alcohol and deionized water for $10\,\text{min}$ each, and then dried at room temperature. For cytocompatibility, sterilization by ultraviolet-radiation for $2\,$ h was conducted for each side of the samples.

During the MAO treatment, a pulse power supply (Xi'an Jiaotong University, China) was applied with a Zn disc as anode and a stainless steel plate as cathode. The electrolyte consisted of 2.5 g/L sodium hydroxide and 0.02 mol/L calcium glycerophosphate hydrate dissolved in deionized water. The pulse frequency was fixed at 500 HZ, and the duty ratio was set as 7.5%. The applied voltage was 100, 200, 300, and 400 V with a treatment time of 3 min, respectively. On the basis of the applied potential, samples were named after MAO100, MAO200, MAO300, and MAO400, respectively. All samples were rinsed with deionized water and dried at ambient temperature. In this work, the samples used in electrochemical corrosion, static immersion, and biocompatibility tests were MAO treated at 400 V, unless a specific statement is pointed out.

2.2. Microstructure and Composition Characterization. SEM (S-4800 Emission Scanning electron microscopy, Hitachi, Japan) equipped with energy dispersive X-ray spectrometer was employed to observe the surface, cross-section morphologies and analyze the elements distribution. The phase composition was identified by X-ray diffraction (XRD, Rigaku DMAX 2400, Japan) using Cu K_{α} radiation at a scan rate of 4 deg/min between 2θ of 10° and 90° at 40 kV and 100 mA.

2.3. Characterization of Bonding Strength of the Coating. The scratch tests with an auto scratch coating tester was employed to

investigate the bonding strength of MAO coatings on pure Zn discs. During the testing process, a spherical stylus (Rockwell C diamond) slid across the coating surface at a constant speed under a loading rate of 50 N/min to generate a scratch. The smallest load, at which a recognized failure happened, is defined as the critical load which was detected to verify the bonding strength of MAO coating according to the curve of acoustic output versus load. Three duplicate samples were utilized to determine the bonding integrity of MAO coating fabricated under different voltage.

2.4. Electrochemical Measurements. The electrochemical test was conducted in a classical three-electrode system including a platinum counter electrode, a saturated calomel electrode (SCE) as reference electrode and a disk-shaped sample with an exposed area of 0.28 cm² as working electrode. The tests were performed in Hank's solution (NaCl 8.00 g·L⁻¹, KCl 0.40 g·L⁻¹, CaCl₂ 0.14 g·L⁻¹, NaHCO₃ 0.35 g·L⁻¹, glucose 1.00 g·L⁻¹, MgCl₂·6H₂O 0.10 g·L⁻¹, $MgSO_4.7H_2O$ 0.06 $g\cdot L^{-1}$, $Na_2HPO_4.12H_2O$ 0.06 $g\cdot L^{-1}$ and KH_2PO_4 $0.06~{\rm g\cdot L^{-1}}$, pH 7.4) using an electrochemical working station (Autolab, Metrohm, Switzerland) at ambient temperature. Each sample was subjected to 5400 s open circuit potential (OCP) measurement. Thereafter, potentiodynamic polarization scans were performed at a scanning rate of 1 mV/s. An average of 5 samples were used for each test. Corrosion potential (E_{corr}) and corrosion current density (Icorr) were estimated based on the Tafel regions of the polarization curve

2.5. Static Immersion Test. The static immersion tests were conducted in Hank's solution according to ASTM G31-72. The exposure ratio of sample was set at 1 cm²: 20 mL at 37 °C by water bath. After 1, 4, 7, 14, 21, and 28 days of immersion, samples were collected, rinsed with deionized water, and dried in air. XRD and SEM equipped with EDX were employed to investigate the changes of surface morphologies and composition. The pH values were measured every day by pH meter. Inductively coupled plasma atomic emission spectrometry (ICP) was utilized to examine the ion concentration of each sample immersed in Hank's solution.

2.6. Indirect Cell Viability and Proliferation Evaluation. The human osteoblast-like cell line (MG63 cell) was utilized to access the cytocompatibility by means of indirect contact assay. MG63 cells were cultured in minimum essential media/Earle's balanced salts (MEM/ EBSS) supplied with 10% fetal bovine serum (FBS), 1% MEM nonessential amino acids, $100 \text{ U} \cdot \text{mL}^{-1}$ penicillin, and $100 \mu \text{g} \cdot \text{mL}^{-1}$ streptomycin in a humidified atmosphere incubator with 5% CO2 at $37\,$ °C. Extracts were generated by using MEM serum free medium with the extraction ratio at 1.25 mL·cm⁻² under standard cell culture condition for 72 h. Afterward, the supernatant fluid from each incubated sample was collected, centrifuged and stored at 4 °C before use. The cell culture medium with and without 10% dimethyl sulfoxide (DMSO) were adopted as positive and negative control, respectively. Cells were seeded in 96-well cell culture plates at a density of 5×10^3 cells per 100 μ L medium. After 24 h of incubation to allow attachment, cell culture medium was superseded with extracts of different concentration and incubated for 1, 3, and 5 days, respectively. Then the cell culture medium with 10% Cell Counting Kit-8 (CCK8, Dojindo, Japan) was substituted for the extracts at defined points and incubated at 37 °C for 1 h. A microplate reader (Bio-RAD680) was utilized to measure the spectrophotometric absorbance of each well at a wavelength of 450 nm. The cell viability was obtained on the basis of the following equation:

2.7. Cell Morphology. For cell morphology and cell-material interaction study, cells were seeded onto each sample in 24-well plates at a density of 5×10^4 cells/well. Afterward, the samples were washed with Dulbecco's phosphate buffered saline (PBS) twice and fixed with 2.5% glutaraldehyde for 2 h after 24 h of incubation. The dehydration process was carried out in gradient ethanol solutions (50%–100%) for 10 min each and then dried at room temperature before use. Cell

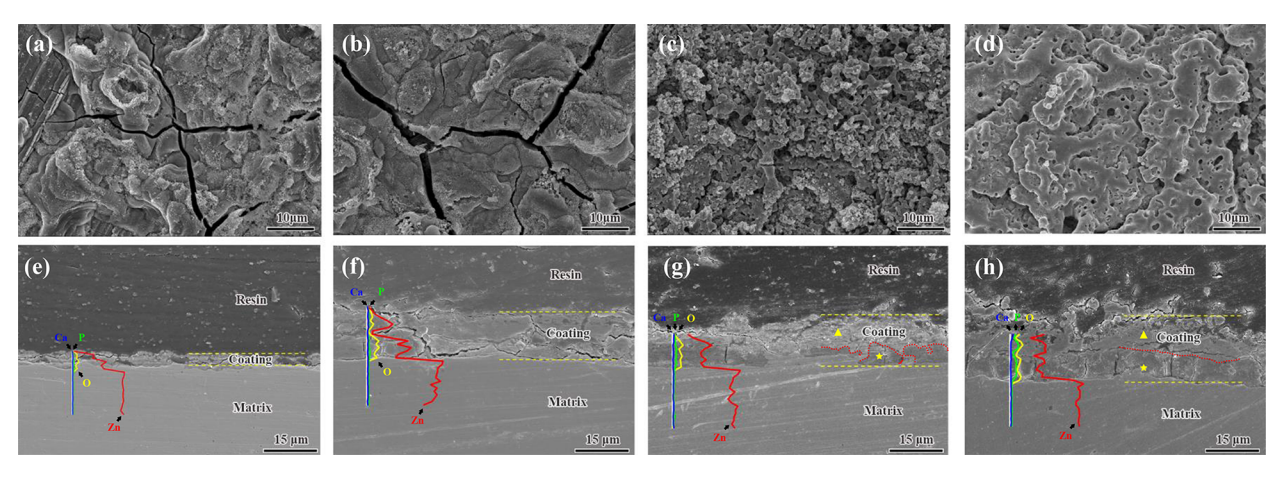


Figure 1. Morphologies of surface (a-d) and cross-section (e-f) of MAO100, MAO200, MAO300, and MAO400, respectively.

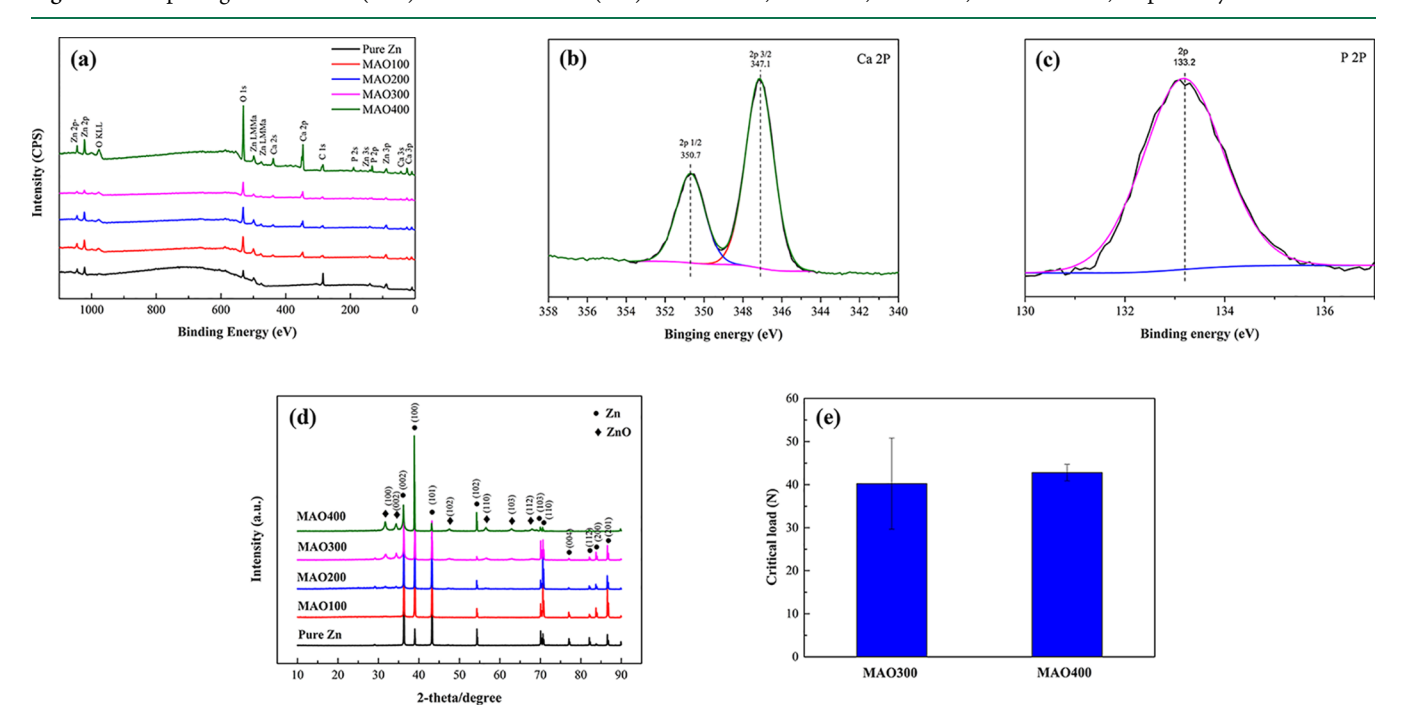


Figure 2. (a) XPS analysis detected on the surface of Zn with and without MAO treatment. High-resolution spectra of (b) Ca 2p and (c) P 2p of MAO400. (d) XRD patterns of pure Zn before and after MAO treatment. (e) The critical load of MAO300 and MAO400 measured by scratch tests.

morphology and attachment were investigated with SEM after being coated with Au.

2.8. MG63 Cell Cycle Analysis. The distribution of cell cycles was evaluated with propidium iodide (PI) staining using the flow cytometer. MG63 cells were seeded into 6-well plates at a cell density of 1×10^5 cells/well and cultured until 80–90% confluence. Prior to use, cells underwent 24 h of serum-starved incubation with MEM/EBSS without FBS. Then cells were treated with 100% extracts for 12 h. After digestion with 0.25% trypsin, cells were harvested by centrifugation and fixed in ice-cold 70% ethanol. RNase A was added to process cells in 37 $^{\circ}\text{C}$ and then cells were stained with PI in dark before analysis.

2.9. Flow Cytometry Analysis of Apoptotic Cells. The influence of the extracts on the MG63 cell apoptosis was carried out with an AnnexinV-FITC Apoptosis detection kit (KeyGEN bioTECH). Cells under different conditions such as normal cells, early apoptotic cells as well as late apoptotic cells can be detected by this test using flow cytometer. The assay was carried out based on the manufacturer's protocol. Briefly, 1×10^5 MG63 cells were seeded in 6-well plates. The culture medium was replaced with 100% extract

after 24 h of incubation, and then the cells were incubated for 8 h. After digestion with 0.25% trypsin, cells were collected and rinsed twice with precooled PBS. Thereafter, cells were resuspended in 500 μ L of binding buffer, which was then supplemented with 10 μ L of annexinV-FITC conjugate and 10 μ L of PI working reagent. Afterward, the cells were incubated at ambient temperature for 15 min and analyzed by flow cytometry.

During the period of apoptosis, the translocation of phosphatidylserine-residues from the inner to the outer cell membrane can be detected by annexinV-FITC. Apoptotic cells are characterized by integrated plasma membrane during a primary part of apoptotic process and turn permeable during secondary necrosis. PI can only stain cell nuclear DNA with permeable cell membranes. Hence, living cells are negative for both annexinV-FITC and PI, apoptotic cells are positive for annexinV-FITC and negative for PI, and dead cells (necrotic cells and apoptotic cells) are positive for both annexinV-FITC and PI.

2.10. Statistical Analysis. Data were expressed as mean \pm standard deviation in this work. Statistical analysis was conducted with SPSS 18.0 software (SPSS Inc., Chicago, USA). One-way

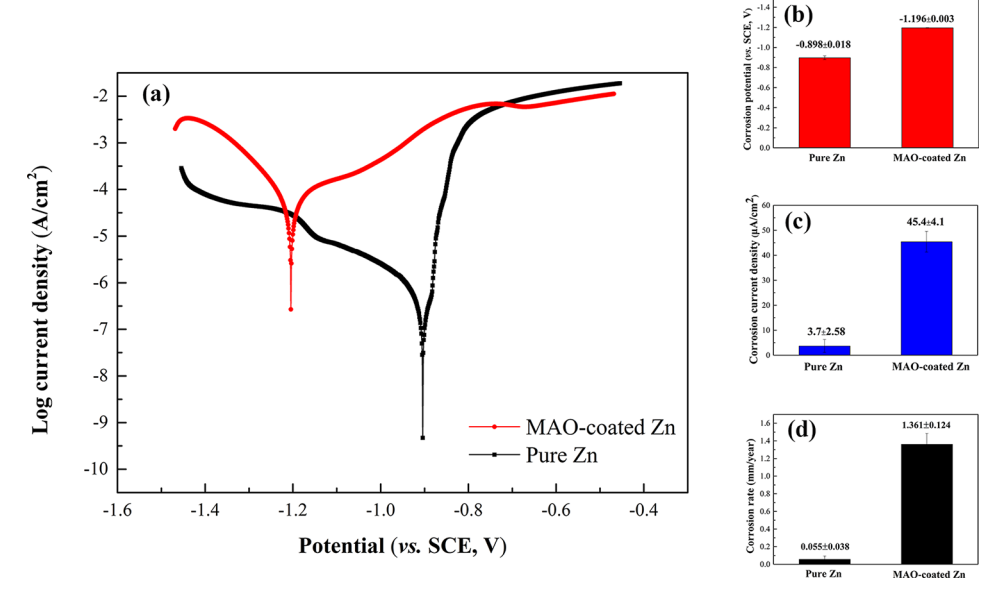


Figure 3. (a) Potentiodynamic polarization curves of pure Zn and MAO-coated Zn in Hank's solution. (b) Corrosion potential (E_{corr}) , (c) corrosion current density (I_{corr}) , and (d) corrosion rate values calculated from the electrochemical tests.

analysis of variance (ANOVA), followed by Tukey post hoc tests was applied to assess the differences between groups. Values of p < 0.05 were considered statistical significant difference.

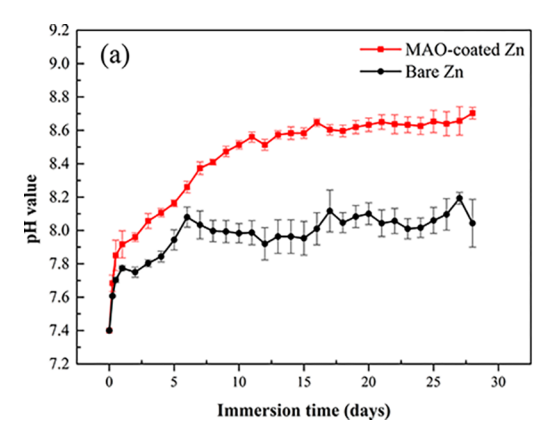
3. RESULTS

3.1. Formation and Structure of MAO Coating. The surface and cross-section morphologies of the MAO-treated samples fabricated under different voltages on pure Zn are displayed in Figure 1. The thickness of coating increased with the rise of applied voltage. In terms of the coating fabricated under 100 and 200 V, numerous cracks were formed across the surface and all depths of the coating by reason for mechanical stress induced by oxide growth and oxygen evolution, whereas no porous structure can be observed as exhibited in Figure 1a, b, e, and f. The anodic film on MAO100 was thin and not compact. A nearly complete coverage was achieved with regard to MAO200. As the applied voltage continued to increase and surpassed the dielectric breakdown voltage, uniformly distributed microarcs can be observed on the surface.27 As a result, a foam-like structure was presented over the MAO coating with plenty of homogeneously distributed pores ranging from submicron scale to several micrometers as shown in Figure 1c and d. The ejectment of the molten oxide and gas bubbles through the microarc discharge channels resulted in the formation of micropores. 28,29 Meanwhile, instead of the tremendous cracks observed on the surface of MAO100 and MAO200, only microcracks can be observed in both top surface and crossing-sectional view, which were generated by the relieved thermal stress in the quenching of the molten oxide by the surrounding electrolyte.²⁸ Nonetheless, there was no obvious interruption between the coating and Zn substrate. The absence of the large cracks may be contributed to the repairmen by molten oxide generated during discharge process. When the applied voltage was 300 V, the coating thickness was about 20 μ m, and a double-layer structure was observed with an outer porous layer (marked by yellow triangle) and an inner dense layer with less porosity (marked by yellow stars) as exhibited in Figure 1c and g. Nonetheless, the inner dense layer was not coherent. The

surface exhibited a relatively coarse appearance with nanopores all over the surface. Subsequently, as the voltage increased to 400 V, the coating turned smooth with an increased thickness of approximately 25 μ m as shown in Figure 1d and h. The thickness of the inner dense layer was also improved in spite of the remaining phenomenon of discontinuity. The bonding strength between the coating and substrate was studied for MAO300 and MAO400, and a superior cohesive strength was demonstrated for coating fabricated in 400 V as shown in Figure 2e.

As identified by EDS spectra, the MAO coating mainly consisted of Zn, O, Ca, and P (Figure 1e-h). The phase components of Zn substrate before and after MAO treatment were revealed by the XRD pattern in Figure 2d. ZnO was generated during the MAO process due to the reaction between the ionized Zn and the O²⁻/OH⁻ anions stemming from the absorbed water dissociation. 25,26 However, the peaks corresponding to the crystallized component consisting of Ca and P were not identified. It is hypothesized that Ca and P may exist in the matrix in the form of amorphous state because of rapid solidification by relatively cool electrolyte. 30 As shown in Figure 2a-c, XPS full spectrum and high-resolution spectra of Ca 2p and P 2p detected from MAO400 coating demonstrated that Ca 2p peaks were assigned to 347.1 (2p3/2) and 350.7 eV (2p1/2), consistent with the Ca 2p in $Ca_3(PO_4)_2$. Meanwhile, the peak of P 2p was detected at 133.2 eV, in accordance with that in Ca₃(PO₄)₂.²⁰ The Ca 2p and P 2p peaks in MAO100, MAO200 and MAO300 were identical to those of MAO400. Therefore, it is implied that Ca and P were incorporated into MAO coating in the form of Ca^{2+} and PO_4^{3-} .

3.2. Electrochemical Evaluations. The potentiodynamic polarization curve measurements of samples with and without MAO treatment in Hank's solution are displayed in Figure 3. In comparison to pure Zn sample, the corrosion potential of MAO-coated sample shifted negatively, suggesting an impaired effect of MAO treatment on Zn. Corrosion parameters, including $E_{\rm corr}$ and $I_{\rm corr}$ extrapolated from potentiodynamic polarization curve, are summarized in Figure 3b–d. The current density increased approximately 1 order of magnitude



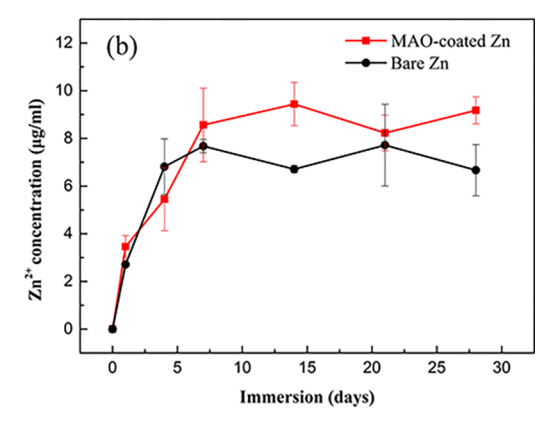


Figure 4. Changes of (a) pH value and (b) Zn²⁺ concentration in Hank's solution during 28 day's immersion.

from 3.7 \pm 2.58 to 45.4 \pm 4.1 μ A·cm⁻². The $E_{\rm corr}$ was decreased as well. The corrosion rates were calculated from current density. Corresponding to the results of $E_{\rm corr}$ and $I_{\rm corr}$, MAO treatment led to a faster corrosion of Zn in Hank's solution from 0.055 \pm 0.038 to 1.361 \pm 0.124 mm·year⁻¹.

3.3. Immersion Tests. Figure 4 displays the variations in pH and Zn ions concentration during 28 days' immersion in Hanks's solution. The corrosion process of pure Zn proceeds via an electrochemical reaction involving the below mentioned anodic oxidation of Zn and cathodic reduction of oxygen under the condition of nearly neutral physiological media: ³¹

anodic reaction

$$Zn \rightarrow Zn^{2+} + 2e^{-} \tag{1}$$

cathodic reaction

$$2H_2O + O_2 + 4e^- \rightarrow 4OH^-$$
 (2)

overall reaction

$$2Zn + 2H_2O + O_2 \rightarrow 2Zn(OH)_2$$
 (3)

Therefore, the evolution of pH and Zn ions concentration can be utilized to evaluate the degradation behavior in Hank's solution. As displayed in Figure 4a, the pH value of MAO-coated Zn increased to 8.70 in the end of immersion, demonstrating a higher reactivity in Hank's solution compared with pure Zn (pH value of 8.04). In accordance with the trend of pH, a higher releasing concentration of Zn ions was observed for MAO-treated Zn (Figure 4b).

The surface morphologies of coated and uncoated samples during 28 days' immersion in Hanks' solution are exhibited in Figure 5. There was no apparent corrosion observed on the surface of bare Zn excepted for the formation of some limited micro cracks in the late period of immersion because of shrinkage of corrosion products during dehydration (Figure 5e and f). In spite of 28 day's immersion, surface scratch formed by mechanical polish can still be observed. Besides, a relatively compact layer was generated during 28 days' immersion (Figure 6a). Interestingly, although the surface showed no obvious variation with regard to MAO-coated sample in the period of 28 days' immersion (Figure 5g—l), the coating suffered serious delamination in the view of cross-section morphology (Figure 6b).

As shown in Figures 6 and 7, the composition of bare and MAO-coated Zn were identified by EDS and XRD after 28 days' immersion. It is found that apparent aggregation of calcium and phosphate can be observed on the surface of

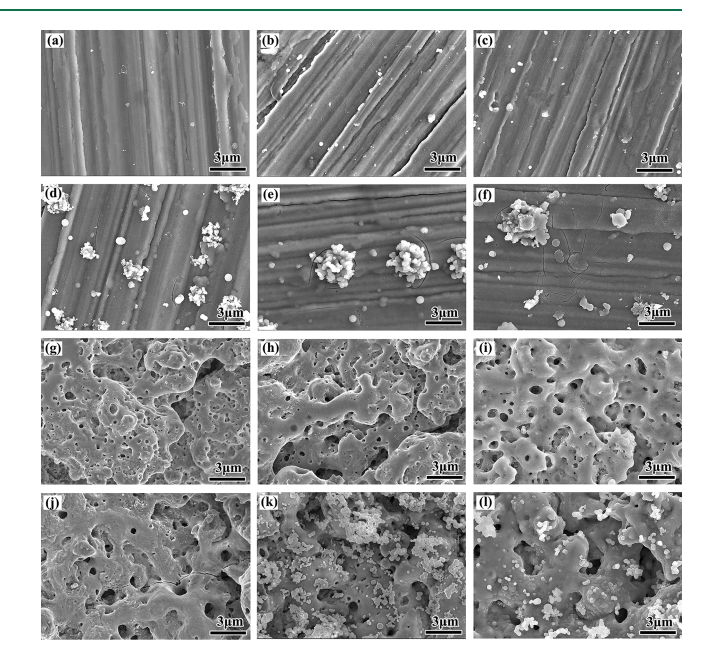


Figure 5. Surface morphologies of (a–f) bare and (g–l) MAO-coated Zn after immersion in Hank's solution for 1, 4, 7, 14, 21, and 28 days, respectively.

MAO-coated Zn (Figure 6b). XRD results revealed that the dominant component of the surface was ZnO, as well as the existence of CaCO₃ (Figure 7b). As for bare Zn, the peaks of ZnO and CaCO₃ were also found in XRD results (Figure 7a). However, there was no prominent enrichment of calcium and phosphate on the surface in contrast to the MAO-coated sample according to the EDS mapping (Figure 6a).

3.4. In Vitro Cytocompatibility. The viabilities of MG63 cells cultured in the extract medium of samples with and without MAO treatment are displayed in Figure 8a. For 100% extracts, both groups exhibited obvious cytotoxicity. Thereinto the extract of MAO-coated sample decreased the cell viability to lower than 12% in contrast to that of 50%–60% for the pure Zn counterpart. In the following 5 day's incubation, the cell viability kept on deteriorating. In spite of the toxic influence observed in the 100% extract groups, excellent cytocompatibility and even salutary influence was attached to the 20% extract groups.

This toxic phenomenon of the 100% extracts may be contributed to the high Zn^{2+} concentration in the extract. As exhibited in Figure 8c, the pH values of the extracts of pure Zn

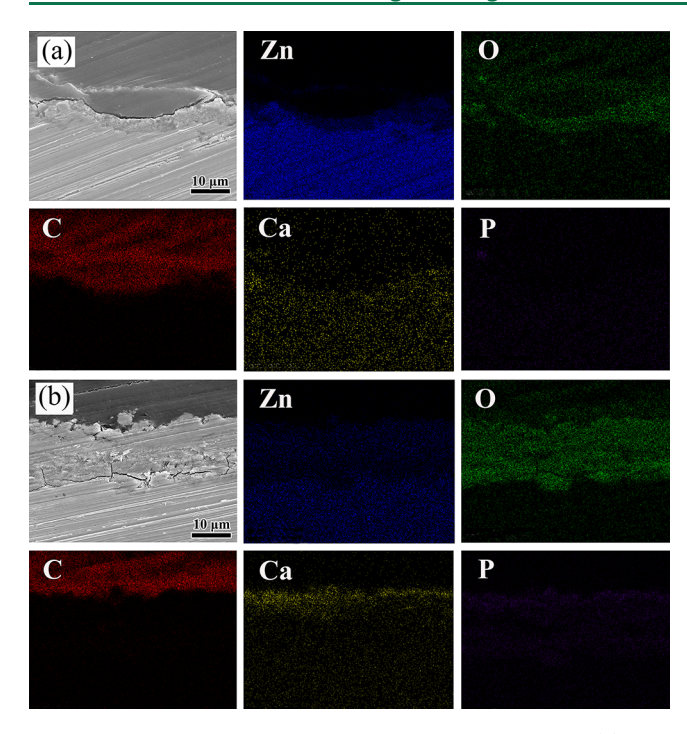


Figure 6. Cross-section morphologies and EDS mapping of (a) bare and (b) MAO-coated Zn after immersion in Hank's solution for 28 days. Maps of zinc, oxygen, carbon, calcium, and phosphate are in blue, green, red, yellow, and purple, respectively.

and MAO-coated Zn were 7.99 and 8.05, respectively. Several researches have implied that an appropriate alkaline microenvironment (pH 8.0–8.5) was beneficial to the proliferation and differentiation of osteoblast cells. ^{32,33} Nonetheless, the concentrations of Zn^{2+} in the extracts of pure Zn and MAO-coated Zn groups were 5.51 and 9.00 μ g/mL, respectively (Figure 8b). Zn²⁺ is capable of inhibiting of the electron transport in the uncoupled mitochondrial. ³⁴ The accumulation of Zn²⁺ gives rise to cell injury. ³⁵ Furthermore, it has been claimed that Zn²⁺ can induce biphasic response to cell viability, adhesion, proliferation, migration of human aorta smooth, and primary human coronary artery endothelial cells in a dose-dependent manner. The high doses of Zn²⁺ generally brought about an adverse effect, while the low doses resulted in the opposite consequence. ^{36,37} The analogically biphasic influence

of Zn²⁺ on L929 and U-2 OS cells were also reported by Kubásek et al. Meanwhile, they found that 100%, 75%, and 50% extracts of Zn-0.8 Mg alloy exhibited a detrimental influence on the cell viability of L929 cells, whereas the 25% extracts generated a beneficial impact.³⁸ Murni et al.³⁹ also reported that the extract of pure Zn powder descended the viability of NHOst primary cells with a concentration of 0.75 mg powder/mL. Recent researches have suggested that a diluted extract should be adopted for the biosafety evaluation of biodegradable metals in consideration of the distinct diversity between the in vitro and in vivo environment. Wang et al. 40 put forward that a dilution ratio ranging from 6 to 10 should be implemented for in vitro cytotoxicity test of Mg-based alloy in bone-rich region on account of the discrepancy between in vitro rapid accumulation of degradation products and in vivo dilution via circulation and metabolism. Fischer et al.⁴¹ recommended a 10-times dilution to adjust the osmolality for cytotoxicity evaluation. In this research, a 5-times dilution was conducted and demonstrated an excellent biocompatibility.

The morphologies of MG63 cells cultured on the surface of pure Zn and MAO-coated Zn are exhibited in Figure 8d–i. Differences in response to untreated and MAO-treated samples were apparent. Cells adhered on the surface of pure Zn samples mainly presented an unhealthy state with rounded shape. Nonetheless, cells displayed an extended morphology with several pseudopodia contacting the substrate after MAO treatment. The superior cell adhesion on MAO-coated samples was ascribed to the nature of rough and porous structure. Colon et al.⁴² reported that increased surface roughness promoted human osteoblasts adhesion on the surface of TiO₂ and ZnO. Deligianni et al.⁴³ investigated the influence of surface roughness of hydroxyapatite on the cell adhesion, proliferation, and detachment of human bone marrow cell and found an ascending trend with the roughness increasing.

The impact of 100% extracts of the bare and MAO-treated samples on the cell cycle distribution was evaluated by flow cytometry as shown in Figure 9a–d. The proportion of cells in G0/G1, S, and G2/M phases of the cell cycle were analyzed. The cell cycle progression is featured by the synthesis and duplication of DNA before division. On the basis of the amount of DNA in the cell nucleus, cells go through three stages of cell cycle: G0/G1, S, and G2. Among these stages, G0/G1 contains one set of DNA, G2/M consists of duplicate

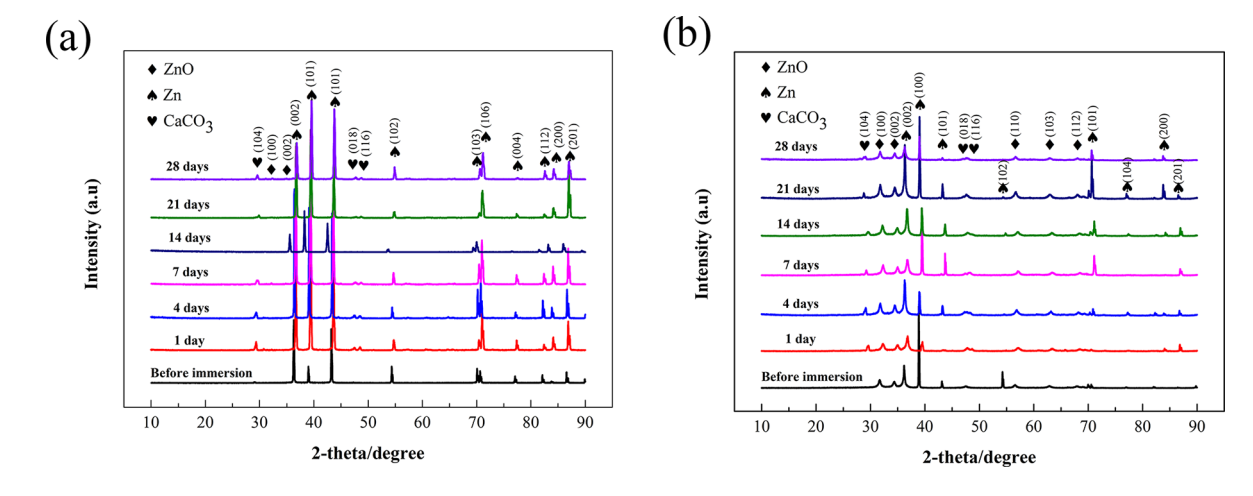


Figure 7. XRD pattern of (a) bare and (b) MAO-coated Zn after immersion in Hank's solution for 1, 4, 7, 14, 21, and 28 days.

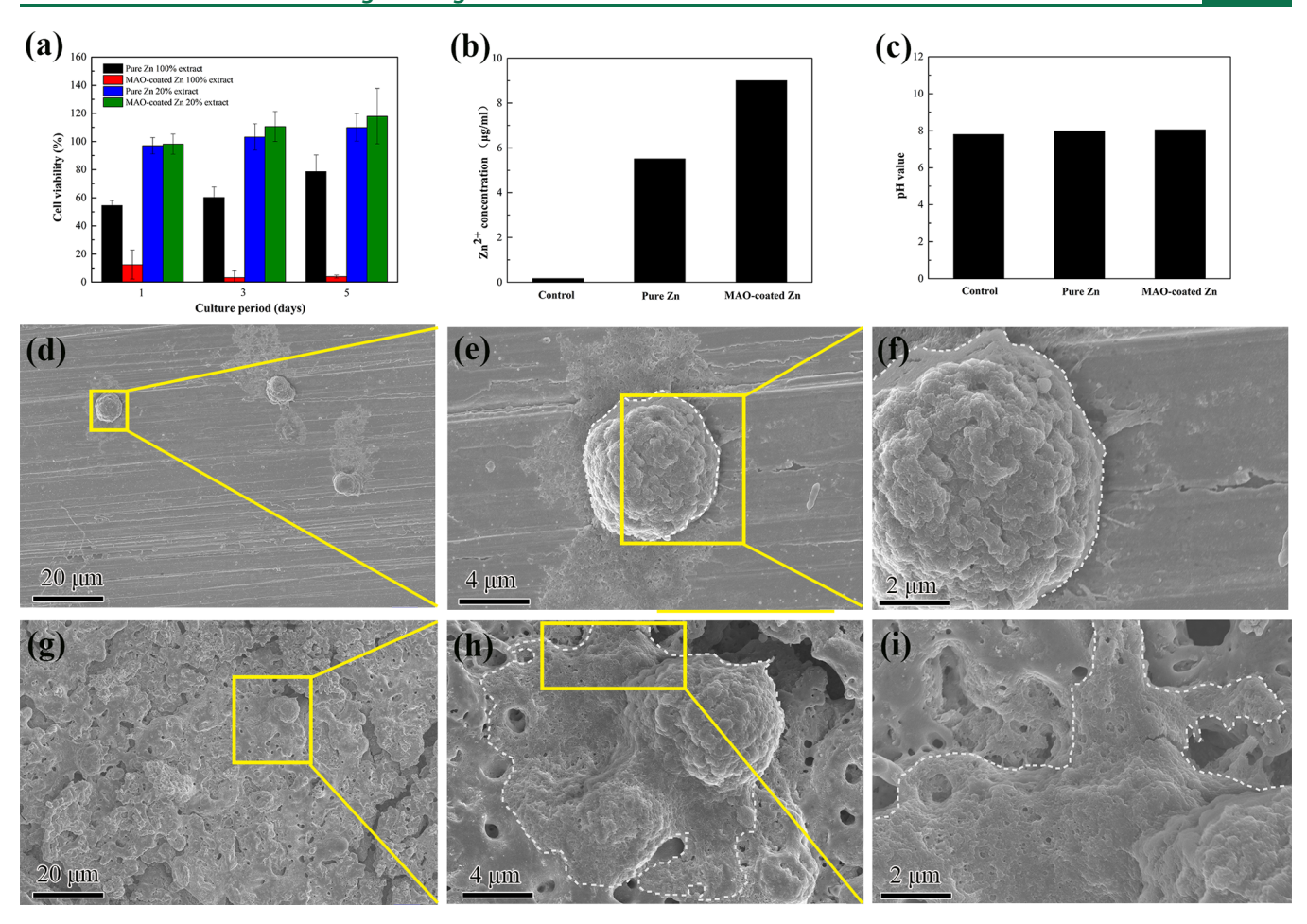


Figure 8. (a) Viability of MG63 cells cultured in the extracts of bare and MAO-coated Zn. (b) Zn^{2+} concentration in the extract media. (c) pH value of the extract media. The morphology of MG63 cells cultured on (d-f) bare and (g-i) MAO-coated Zn. The green color in panels d and g represents cells, and the dotted line refers to the interface between cells and materials in panels e, f, h, and i.

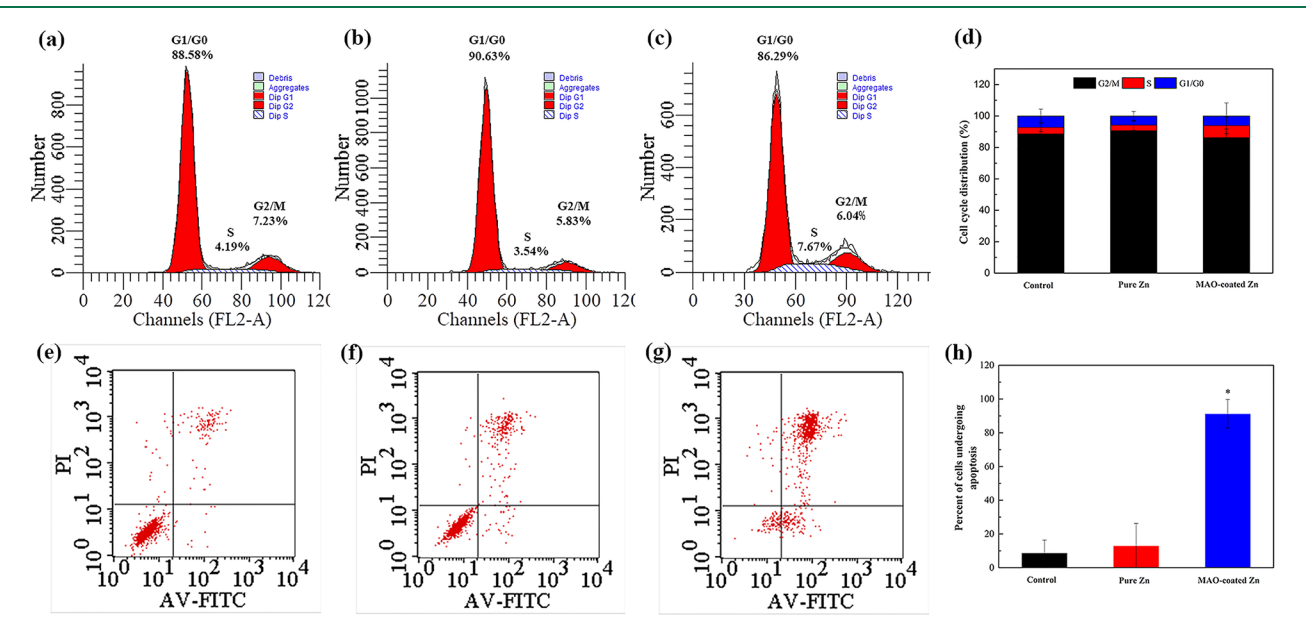


Figure 9. Influence of 100% extracts on the cell cycle progression of MG63 cells: (a) control group, (b) pure Zn, (c) MAO-coated Zn, and (d) graphic representations of the cell cycle distributions. Cell apoptosis analysis of MG63 cells cultured in the 100% extract of (e) control group, (f) pure Zn, (g) MAO-coated Zn, and (h) diagrammatic illustration of the cell apoptosis rate.

set of DNA, and an intermediate amount is presented in S.⁴⁴ The cell cycle analysis data illustrated that the percentage of

MG63 cells in S and G2 for MAO-coated Zn group was obviously higher compared with the pure Zn group and control

ACS Biomaterials Science & Engineering

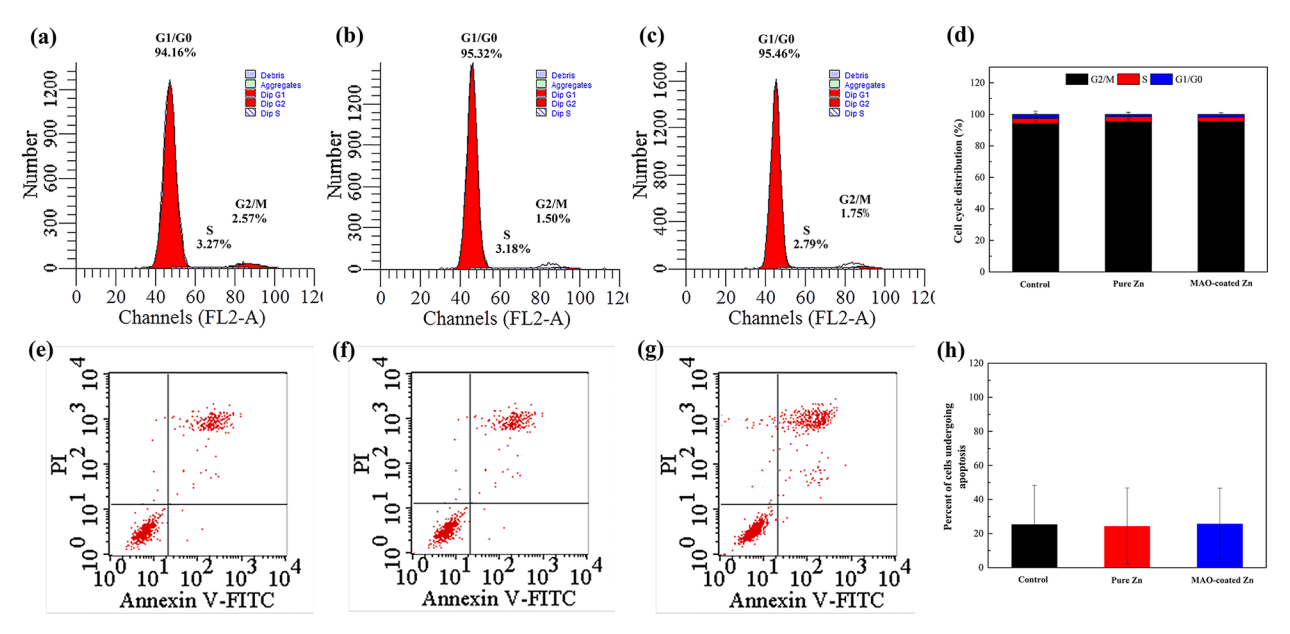


Figure 10. Influence of 20% extracts on the cell cycle progression of MG63 cells: (a) control group, (b) pure Zn, (c) MAO-coated Zn, and (d) graphic representations of the cell cycle distributions. Cell apoptosis analysis of MG63 cells cultured in the 20% extracts of (e) control group, (f) pure Zn, (g) MAO-coated Zn, and (h) diagrammatic illustration of the cell apoptosis rate.

group, indicating that high concentration of Zn²⁺ in the extract of MAO-coated Zn had a positive effect on the cell cycle progression. The verification of the mechanism of cell injury/ death induced by biomaterials has a significant effect on the assessment of the physiological response to biomedical implants. Apoptosis is a specialized form of cell death requiring active gene expression under the condition of specific development and environmental stimuli. A flow cytometry was carried out to study the apoptosis rate of MG63 cells cultured in the extracts of untreated and MAO-treated samples as shown in Figure 9e-h. The percentage of apoptotic cell was $13.09 \pm 13.15\%$ and $91.32 \pm 8.44\%$ for pure Zn group and MAO-coated Zn group, respectively (Figure 9h). Therefore, higher dose of Zn²⁺ had a more severe apoptotic effect on MG63 cells. In contrast, no apparent changes took place in cell cycle and apoptosis for cell cultured in the 20% extracts of both bare and MAO-coated Zn compared with control group, as shown in Figure 10.

It is claimed that Zn can stimulate osteoblast proliferation and mineralization, exhibiting an anabolic effect on bone metabolism. Meanwhile, Zn is beneficial to osteoblast marker gene expression along with calcium deposition.⁴⁵ Plenty of researches have demonstrated that incorporation of Zn with appropriate dosage can promote cell adhesion, proliferation and differentiation of osteoblast-like cell in addition to bone formation in vitro or in vivo. 46,47 Moreover, it is reported that the high dose of Zn2+ had a detrimental effect on the cell viability.³⁸ The influence of Zn²⁺ on the cell cycle progression and cell apoptosis was dose-dependent and mutually independent. Exposure to 200 μ M Zn²⁺ led to suppression of cell cycle progression while no obvious effect was observed on cell apoptosis.⁴⁸ In addition, no significant change on cell cycle but promotion of cell apoptosis was found under the high concentration of Zn²⁺ in terms of HepG2 cells.⁴⁸ The results exhibited in Figure 9 implied that high Zn²⁺ concentration can provoke growth and apoptosis of MG63 cell simultaneously. However, the aureole of cell apoptosis sheltered the progress of cell cycle, resulting in the deterioration of cell viability (Figure

8a). The molecular mechanism of how ${\rm Zn^{2+}}$ participate in the process of MG63 cell cycle and apoptosis is still unclear.

Therefore, further researches need to be conducted in the future.

4. DISCUSSION

4.1. Comparison of the Formation Mechanism of MAO Coating between Mg and Zn. MAO has been wildly applied to Mg-based alloys as an effective surface modification method and has been proved to result in a remarkable improvement on the corrosion resistance of Mg alloys in the initial degradation period.⁴⁹ A double-layer structure made up of an outer porous layer and an inner compact layer was constructed during MAO process in terms of Mg alloys. 23,50 On the basis of the voltage range, the formation process of MAO coating on Mg can be divided into different stages: (1) First, a thin and compact oxide film (barrier layer) is generated on the surface under a relatively low anodic voltage as shown in Figure 11a. No sparks can be observed in this step.⁵¹ (2) When the voltage rises and strides over the threshold of breakdown voltage, the loss of dielectric stability results in the formation of discharge channels in the low dielectric region.⁵² As a consequence, numerous microsparks are generated in the thinner or weaker spots and move rapidly over the oxide film. Despite that the lifetime of each spark is no more than 1 ms,⁵³ the local temperature of approximate 2000-10000 K at the discharge channels is able to bring about the formation of anodic film and melt of substrate.⁵² A portion of melt erupts along the discharge channels and the melted products deposited on the discharge channel walls when the melt is cooled down by the electrolyte. In this manner, the coating thickness increases and porous structure comes into being (Figure 11b). During the growth process of MAO coating, the compact inner layer comes into being at the beginning stage of discharge sparking when the voltage surpasses the breakdown

Comparing with Mg, the formation of MAO coating on Zn shares a semblable process. A thin anodic film forms at the

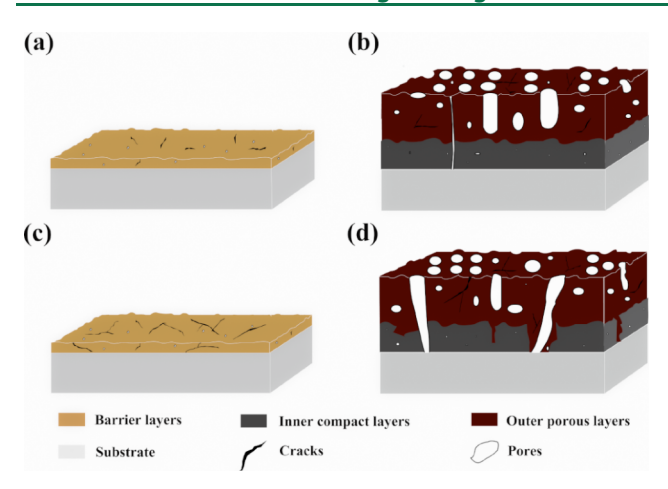


Figure 11. Schematic diagram of the structural characteristics of MAO coating formed in low voltage (blow breakdown voltage) and high voltage (above breakdown voltage) on (a, b) Mg and (c, d) Zn, respectively.

initial stage. Subsequently, a thick and porous coating is generated when the voltage increase above the breakdown voltage. Nonetheless, the compact inner layer is missing in terms of MAO treatment on Zn (Figure 11d). It is reported that in the initial stage before the spark anodization, a barrier layer can be formed on the surface in terms of valve metals such as titanium, magnesium, aluminum, etc., while such compact passive oxide layers are absent in terms of nonvalve metal, such as iron, steel, zinc, etc. As observed in this research, the anodic film formed in low voltage is loosened with many cracks and pores distributed over the cross section (Figure 11c). Therefore, it is hypothesized that these defects in the anodic film formed in low voltage result in the incoherent dense inner structure under the circumstance of high gas release and microarcs in the initial sparking discharge sparking period.

4.2. Comparison of the Corrosion Behavior between MAO-Coated Mg and Zn. Two types of models have been put forward to elucidate the corrosion mechanism of Mg alloys after MAO treatment, namely, the chemical dissolution model and electrochemical corrosion model.⁵⁶ The former involves the gradual degradation of the outer porous structure and the subsequent deterioration of the inner dense structure. In physiological media, the outmost surface of MAO-coated Mg alloy will react with corrosive solution in the first place. As corrosion continues, corrosive solution gets through the out layer and contacts with the inner dense layer and interface layer with larger pores coming into being in the out layer. Once the media hits on the interface, the corrosion of substrate will get easier. 57,58 In the corrosion process mentioned above, the inner compact layer is declared to play a dominant role in the protective function of MAO coating as a continuous barrier against charge transport and the following degradation.⁵⁹ Otherwise, electrochemical corrosion model refers to the galvanic corrosion between the MAO coating and the substrate. The through-pores and microcracks generated in the MAO treatment provides access for corrosion media to be transported into the substrate and formed local galvanic cell.

In consideration of the structural differences of MAO coating between Mg and Zn, the compact inner layer can provide an excellent physical isolation of Mg substrate from corrosion media at the beginning of immersion. Nevertheless,

the existence of microcracks and discontinuity of the inner layer fails to provide sufficient and potent protection against the corrosion media in the case of MAO coating on Zn. Hence, the chemical dissolution process of Zn substrate will speed up in comparison to Mg. Besides, ZnO, the primary component of MAO coating, has been reported to be more stable than Zn in 0.1 M sodium chloride solution under neutral and alkaline condition. The abundant cracks and through-pores in MAO coating on Zn make it easier for the corrosion media to contact with the interface between the coating and substrate, thus resulting in more local galvanic corrosion between Zn substrate and coating (Figure 12b). Rocca et al. investigated the

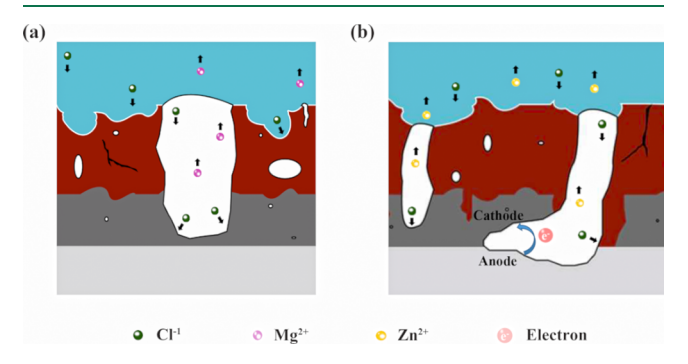


Figure 12. Schematic diagram of the corrosion behavior of MAO-coated (a) Mg and (b) Zn during the initial immersion period in the simulated body fluid.

electrochemical behavior of pure Zn during MAO process in KOH electrolyte. The researchers observed a completely exfoliated structure of the MAO coating because of the mechanical action of oxygen bubbling and microarcs discharge, resulting in a poor protection against corrosion. As a consequence, an accelerated corrosion rate can be expected for the MAO-coated Zn in contrast to the protective effect of MAO coating on Mg as displayed in Figure 12.

Generally, the ideal biodegradable metal devices are expected to possess sufficient mechanical support and degradation. Especially, the evolution of these two variables should comply with the healing process of injured tissue which strongly depends on the selected material and implanted site. In terms of cardiovascular stent application, the mechanical integrity should remain in the first 4 months followed by gradual degradation. As for the bone application, the corresponding time period is 3-6 months. Yang et al. 22 implanted pure Zn stent into the abdominal aorta of the Japanese rabbits. The results showed that the volume loss of the zinc stents was only 20 \pm 2.81% and 41.75 \pm 29.72% at 6 and 12 months. The volume loss of pure Zn was 1.7% when implanted in the rat femur condyle after 2 months implantation.¹² Therefore, a stepped-up corrosion rate may be beneficial in case of complications of long-term retention. 63,64

5. CONCLUSIONS

The MAO coatings prepared in electrolyte containing calcium and phosphorus component on the high-purity Zn at different voltage have been systematically investigated. The difference between Mg and Zn in the formation mechanism and corrosion performance after MAO treatment are discussed. The conclusions are drawn as follows: (1) Porous MAO coating consisting of ZnO and CaP compound has been

successfully fabricated on pure Zn with homogeneously distributed pores varying from submicron scale to several micrometers. The MAO treatment under 400 V might be superior for surface modification on account of the size of porous structure, as well as the cohesive strength of MAO coating. (2) A double-layer structure was generated on MAOtreated Zn with a porous outer layer and an incoherent dense inner layer, in contrast to the compact inner structure constructed on the MAO-treated Mg alloys. (3) The MAO coating may accelerate the corrosion of Zn substrate due to anabatic chemical dissolution and galvanic corrosion between coating and substrate in opposition to the improved corrosion behavior of MAO-treated Mg alloys. (4) Cytotoxicity was detected in 100% extract groups of both pure Zn and MAOtreated Zn, whereas excellent cytocompatibility is found after 5 times dilution. In addition, the porous structure of MAOtreated Zn also promotes cell adhesion compared with untreated Zn.

AUTHOR INFORMATION

Corresponding Authors

*Tel./Fax: 0086-10-62767411. E-mail: yfzheng@pku.edu.cn (Biomaterials).

*E-mail: hanyong@xjtu.edu.cn (Surface Science).

*E-mail: Chendafu@jsthospital.org (Medicine).

ORCID ®

Donghui Zhu: 0000-0002-3057-1889 Yufeng Zheng: 0000-0002-7402-9979

Notes

The authors declare no competing financial interest.

ACKNOWLEDGMENTS

This work was supported by State Key Laboratory for Mechanical Behavior of Materials (Grant No. 20182011), National Natural Science Foundation of China (Grant No. 51431002 and 51871004), NSFC/RGC Joint Research Scheme (Grant No. 5161101031).

REFERENCES

- (1) Zhang, S.; Zhang, X.; Zhao, C.; Li, J.; Song, Y.; Xie, C.; Tao, H.; Zhang, Y.; He, Y.; Jiang, Y.; Bian, Y. Research on an Mg—Zn alloy as a degradable biomaterial. *Acta Biomater.* **2010**, *6* (2), 626—640.
- (2) Yu, J.; Wang, J.; Li, Q.; Shang, J.; Cao, J.; Sun, X. Effect of Zn on Microstructures and Properties of Mg-Zn Alloys Prepared by Powder Metallurgy Method. *Rare Met. Mater. Eng.* **2016**, *45* (11), 2757–2762.
- (3) Cheng, J.; Liu, B.; Wu, Y. H.; Zheng, Y. F. Comparative in vitro Study on Pure Metals (Fe, Mn, Mg, Zn and W) as Biodegradable Metals. J. Mater. Sci. Technol. 2013, 29 (7), 619–627.
- (4) Hambidge, K. M.; Krebs, N. F. Zinc Deficiency: A Special Challenge. J. Nutr. 2007, 137 (4), 1101–1105.
- (5) Moonga, B. S.; Dempster, D. W. Zinc is a potent inhibitor of osteoclastic bone resorption in vitro. *J. Bone Miner. Res.* **1995**, *10* (3), 453–457.
- (6) Ortega, R. M.; Quintas, M. E.; Andrés, P.; Martinez, R. M.; López-Sobaler, A. M.; Requejo, A. M. Zinc status of a group of pregnant Spanish women: effects on anthropometric data and Apgar scores of neonates. *Nutr. Res.* (N. Y., NY, U. S.) 1999, 19 (9), 1423–1428.
- (7) Jin, H.; Zhao, S.; Guillory, R.; Bowen, P. K.; Yin, Z.; Griebel, A.; Schaffer, J.; Earley, E. J.; Goldman, J.; Drelich, J. W. Novel high-strength, low-alloys Zn-Mg (<0.1wt% Mg) and their arterial biodegradation. *Mater. Sci. Eng., C* 2018, 84, 67–79.
- (8) Li, H. F.; Xie, X. H.; Zheng, Y. F.; Cong, Y.; Zhou, F. Y.; Qiu, K. J.; Wang, X.; Chen, S. H.; Huang, L.; Tian, L.; Qin, L. Development

- of biodegradable Zn-1X binary alloys with nutrient alloying elements Mg, Ca and Sr. Sci. Rep. 2015, S, 10719.
- (9) Zhao, S.; Seitz, J. M.; Eifler, R.; Maier, H. J.; Guillory, R. J.; Earley, E. J.; Drelich, A.; Goldman, J.; Drelich, J. W. Zn-Li alloy after extrusion and drawing: Structural, mechanical characterization, and biodegradation in abdominal aorta of rat. *Mater. Sci. Eng., C* 2017, 76, 301–312.
- (10) Drelich, A. J.; Zhao, S.; Guillory, R. J.; Drelich, J. W.; Goldman, J. Long-term surveillance of zinc implant in murine artery: Surprisingly steady biocorrosion rate. *Acta Biomater.* **2017**, *58*, 539–549.
- (11) Kafri, A.; Ovadia, S.; Goldman, J.; Drelich, J.; Aghion, E. The Suitability of Zn-1.3%Fe Alloy as a Biodegradable Implant Material. *Metals* **2018**, *8* (3), 153.
- (12) Yang, H.; Qu, X.; Lin, W.; Wang, C.; Zhu, D.; Dai, K.; Zheng, Y. In vitro and in vivo studies on zinc-hydroxyapatite composites as novel biodegradable metal matrix composite for orthopedic applications. *Acta Biomater.* **2018**, *71*, 200–214.
- (13) Gencer, Y.; Gulec, A. E. The effect of Zn on the microarc oxidation coating behavior of synthetic Al–Zn binary alloys. *J. Alloys Compd.* **2012**, 525, 159–165.
- (14) Han, Y.; Hong, S.-H.; Xu, K. Synthesis of nanocrystalline titania films by micro-arc oxidation. *Mater. Lett.* **2002**, *56* (5), 744–747.
- (15) Yu, H.; Dong, Q.; Dou, J.; Pan, Y.; Chen, C. Structure and in vitro bioactivity of ceramic coatings on magnesium alloys by microarc oxidation. *Appl. Surf. Sci.* **2016**, 388, 114–119.
- (16) Yan, Y.; Han, Y.; Lu, C. The effect of chemical treatment on apatite-forming ability of the macroporous zirconia films formed by micro-arc oxidation. *Appl. Surf. Sci.* **2008**, 254 (15), 4833–4839.
- (17) Zhao, L.; Cui, C.; Wang, Q.; Bu, S. Growth characteristics and corrosion resistance of micro-arc oxidation coating on pure magnesium for biomedical applications. *Corros. Sci.* **2010**, *52* (7), 2228–2234.
- (18) Němcová, A.; Skeldon, P.; Thompson, G. E.; Pacal, B. Effect of fluoride on plasma electrolytic oxidation of AZ61 magnesium alloy. *Surf. Coat. Technol.* **2013**, 232, 827–838.
- (19) Pan, Y. K.; Chen, C. Z.; Wang, D. G.; Zhao, T. G. Effects of phosphates on microstructure and bioactivity of micro-arc oxidized calcium phosphate coatings on Mg–Zn–Zr magnesium alloy. *Colloids Surf., B* **2013**, *109*, 1–9.
- (20) Li, B.; Han, Y.; Qi, K. Formation mechanism, degradation behavior, and cytocompatibility of a nanorod-shaped HA and pore-sealed MgO bilayer coating on magnesium. *ACS Appl. Mater. Interfaces* **2014**, *6* (20), 18258–74.
- (21) Li, Y.; Lee, I. S.; Cui, F. Z.; Choi, S. H. The biocompatibility of nanostructured calcium phosphate coated on micro-arc oxidized titanium. *Biomaterials* **2008**, *29* (13), 2025–2032.
- (22) Hiromoto, S.; Inoue, M.; Taguchi, T.; Yamane, M.; Ohtsu, N. In vitro and in vivo biocompatibility and corrosion behaviour of a bioabsorbable magnesium alloy coated with octacalcium phosphate and hydroxyapatite. *Acta Biomater.* **2015**, *11*, 520–530.
- (23) Fischerauer, S. F.; Kraus, T.; Wu, X.; Tangl, S.; Sorantin, E.; Hänzi, A. C.; Löffler, J. F.; Uggowitzer, P. J.; Weinberg, A. M. In vivo degradation performance of micro-arc-oxidized magnesium implants: A micro-CT study in rats. *Acta Biomater.* **2013**, 9 (2), 5411–5420.
- (24) Cui, X. J.; Lin, X. z.; Liu, C. H.; Yang, R. S.; Zheng, X. W.; Gong, M. Fabrication and corrosion resistance of a hydrophobic micro-arc oxidation coating on AZ31 Mg alloy. *Corros. Sci.* **2015**, *90*, 402–412.
- (25) Stojadinović, S.; Tadić, N.; Vasilić, R. Formation and characterization of ZnO films on zinc substrate by plasma electrolytic oxidation. *Surf. Coat. Technol.* **2016**, *307*, 650–657.
- (26) Rocca, E.; Veys-Renaux, D.; Guessoum, K. Electrochemical behavior of zinc in KOH media at high voltage: Micro-arc oxidation of zinc. *J. Electrognal. Chem.* **2015**, 754, 125–132.
- (27) Gu, X. N.; Li, N.; Zhou, W. R.; Zheng, Y. F.; Zhao, X.; Cai, Q. Z.; Ruan, L. Corrosion resistance and surface biocompatibility of a microarc oxidation coating on a Mg-Ca alloy. *Acta Biomater.* **2011**, 7 (4), 1880–9.

- (28) Sankara Narayanan, T. S. N.; Park, I. S.; Lee, M. H. Strategies to improve the corrosion resistance of microarc oxidation (MAO) coated magnesium alloys for degradable implants: Prospects and challenges. *Prog. Mater. Sci.* **2014**, *60*, 1–71.
- (29) Duan, H.; Du, K.; Yan, C.; Wang, F. Electrochemical corrosion behavior of composite coatings of sealed MAO film on magnesium alloy AZ91D. *Electrochim. Acta* **2006**, *51* (14), 2898–2908.
- (30) Yao, Z.; Li, L.; Jiang, Z. Adjustment of the ratio of Ca/P in the ceramic coating on Mg alloy by plasma electrolytic oxidation. *Appl. Surf. Sci.* **2009**, 255 (13–14), 6724–6728.
- (31) Liu, X.; Sun, J.; Qiu, K.; Yang, Y.; Pu, Z.; Li, L.; Zheng, Y. Effects of alloying elements (Ca and Sr) on microstructure, mechanical property and in vitro corrosion behavior of biodegradable Zn-1.5Mg alloy. *J. Alloys Compd.* **2016**, *664*, 444–452.
- (32) Liu, W.; Wang, T.; Yang, C.; Darvell, W.; Wu, J.; Lin, K.; Chang, J.; Pan, H.; Lu, W. W. Alkaline biodegradable implants for osteoporotic bone defects—importance of microenvironment pH. Osteoporosis Int. 2016, 27 (1), 93–104.
- (33) Tan, J.; Wang, D.; Cao, H.; Qiao, Y.; Zhu, H.; Liu, X. Effect of Local Alkaline Microenvironment on the Behaviors of Bacteria and Osteogenic Cells. ACS Appl. Mater. Interfaces 2018, 10, 42018.
- (34) Kleiner, D. The effect of Zn²⁺ ions on mitochondrial electron transport. *Arch. Biochem. Biophys.* **1974**, *165* (1), 121–125.
- (35) Sensi, S. L.; Ton-That, D.; Sullivan, P. G.; Jonas, E. A.; Gee, K. R.; Kaczmarek, L. K.; Weiss, J. H. Modulation of mitochondrial function by endogenous Zn²⁺ pools. *Proc. Natl. Acad. Sci. U. S. A.* **2003**, *100* (10), 6157–6162.
- (36) Ma, J.; Zhao, N.; Zhu, D. Bioabsorbable zinc ion induced biphasic cellular responses in vascular smooth muscle cells. *Sci. Rep.* **2016**, *6*, 26661 DOI: 10.1038/srep26661.
- (37) Ma, J.; Zhao, N.; Zhu, D. Endothelial Cellular Responses to Biodegradable Metal Zinc. ACS Biomater. Sci. Eng. 2015, 1 (11), 1174–1182.
- (38) Kubásek, J.; Vojtěch, D.; Jablonská, E.; Pospíšilová, I.; Lipov, J.; Ruml, T. Structure, mechanical characteristics and in vitro degradation, cytotoxicity, genotoxicity and mutagenicity of novel biodegradable Zn-Mg alloys. *Mater. Sci. Eng., C* **2016**, 58, 24–35.
- (39) Murni, N. S.; Dambatta, M. S.; Yeap, S. K.; Froemming, G. R.; Hermawan, H. Cytotoxicity evaluation of biodegradable Zn-3Mg alloy toward normal human osteoblast cells. *Mater. Sci. Eng., C* **2015**, 49, 560–6.
- (40) Wang, J.; Witte, F.; Xi, T.; Zheng, Y.; Yang, K.; Yang, Y.; Zhao, D.; Meng, J.; Li, Y.; Li, W.; Chan, K.; Qin, L. Recommendation for modifying current cytotoxicity testing standards for biodegradable magnesium-based materials. *Acta Biomater.* **2015**, *21*, 237–49.
- (41) Fischer, J.; Pröfrock, D.; Hort, N.; Willumeit, R.; Feyerabend, F. Improved cytotoxicity testing of magnesium materials. *Mater. Sci. Eng., B* **2011**, *176* (11), 830–834.
- (42) Colon, G.; Ward, B. C.; Webster, T. J. Increased osteoblast and decreased Staphylococcus epidermidis functions on nanophase ZnO and TiO₂. J. Biomed. Mater. Res., Part A 2006, 78 (3), 595–604.
- (43) Deligianni, D. D.; Katsala, N. D.; Koutsoukos, P. G.; Missirlis, Y. F. Effect of surface roughness of hydroxyapatite on human bone marrow cell adhesion, proliferation, differentiation and detachment strength. *Biomaterials* **2000**, 22 (1), 87–96.
- (44) Mao, J. S.; Cui, Y. L.; Wang, X. H.; Sun, Y.; Yin, Y. J.; Zhao, H. M.; De Yao, K. A preliminary study on chitosan and gelatin polyelectrolyte complex cytocompatibility by cell cycle and apoptosis analysis. *Biomaterials* **2004**, *25* (18), 3973–3981.
- (45) Huo, K.; Zhang, X.; Wang, H.; Zhao, L.; Liu, X.; Chu, P. K. Osteogenic activity and antibacterial effects on titanium surfaces modified with Zn-incorporated nanotube arrays. *Biomaterials* **2013**, 34 (13), 3467–3478.
- (46) Miao, S.; Cheng, K.; Weng, W.; Du, P.; Shen, G.; Han, G.; Yan, W.; Zhang, S. Fabrication and evaluation of Zn containing fluoridated hydroxyapatite layer with Zn release ability. *Acta Biomater.* **2008**, *4* (2), 441–446.

- (47) Lusvardi, G.; Zaffe, D.; Menabue, L.; Bertoldi, C.; Malavasi, G.; Consolo, U. In vitro and in vivo behaviour of zinc-doped phosphosilicate glasses. *Acta Biomater.* **2009**, *5* (1), 419–428.
- (48) Wang, Y. H.; Li, K. J.; Mao, L.; Hu, X.; Zhao, W. J.; Hu, A.; Lian, H. Z.; Zheng, W. J. Effects of exogenous zinc on cell cycle, apoptosis and viability of MDAMB231, HepG2 and 293 T cells. *Biol. Trace Elem. Res.* 2013, 154 (3), 418–26.
- (49) Zhang, L.; Zhang, J.; Chen, C.; Gu, Y. Advances in microarc oxidation coated AZ31 Mg alloys for biomedical applications. *Corros. Sci.* **2015**, *91*, 7–28.
- (50) Lin, X.; Tan, L.; Zhang, Q.; Yang, K.; Hu, Z.; Qiu, J.; Cai, Y. The in vitro degradation process and biocompatibility of a ZK60 magnesium alloy with a forsterite-containing micro-arc oxidation coating. *Acta Biomater.* **2013**, *9* (10), 8631–42.
- (51) Wang, Y.; Wang, J.; Zhang, J.; Zhang, Z. Characteristics of anodic coatings oxidized to different voltage on AZ91D Mg alloy by micro-arc oxidization technique. *Mater. Corros.* **2005**, *56* (2), 88–92.
- (52) Durdu, S.; Usta, M. Characterization and mechanical properties of coatings on magnesium by micro arc oxidation. *Appl. Surf. Sci.* **2012**, *261*, 774–782.
- (53) Xue, W.; Deng, Z.; Chen, R.; Zhang, T. Growth regularity of ceramic coatings formed by microarc oxidation on Al-Cu-Mg alloy. *Thin Solid Films* **2000**, 372 (1–2), 114–117.
- (54) Jiang, J.; Zhou, Q.; Yu, J.; Ma, A.; Song, D.; Lu, F.; Zhang, L.; Yang, D.; Chen, J. Comparative analysis for corrosion resistance of micro-arc oxidation coatings on coarse-grained and ultra-fine grained AZ91D Mg alloy. Surf. Coat. Technol. 2013, 216, 259–266.
- (55) Rudnev, V. S.; Medkov, M. A.; Yarovaya, T. P.; Steblevskaya, N. I.; Nedovzorov, P. M.; Belobeletskaya, M. V. Combination of plasma-electrolytic oxidation and extraction-pyrolytic method for formation of metal oxide layers. *Russ. J. Appl. Chem.* **2012**, 85 (4), 621–628.
- (56) Cui, L. Y.; Zeng, R. C.; Guan, S. K.; Qi, W. C.; Zhang, F.; Li, S. Q.; Han, E. H. Degradation mechanism of micro-arc oxidation coatings on biodegradable Mg-Ca alloys: The influence of porosity. *J. Alloys Compd.* **2017**, *695*, 2464–2476.
- (57) Cai, J.; Cao, F.; Chang, L.; Zheng, J.; Zhang, J.; Cao, C. The preparation and corrosion behaviors of MAO coating on AZ91D with rare earth conversion precursor film. *Appl. Surf. Sci.* **2011**, 257 (8), 3804–3811
- (58) Zeng, R. C.; Cui, L. Y.; Jiang, K.; Liu, R.; Zhao, B. D.; Zheng, Y. F. In Vitro Corrosion and Cytocompatibility of a Microarc Oxidation Coating and Poly(L-lactic acid) Composite Coating on Mg-1Li-1Ca Alloy for Orthopedic Implants. ACS Appl. Mater. Interfaces 2016, 8 (15), 10014–28.
- (59) Gu, Y.; Chen, C.; Bandopadhyay, S.; Ning, C.; Zhang, Y.; Guo, Y. Corrosion mechanism and model of pulsed DC microarc oxidation treated AZ31 alloy in simulated body fluid. *Appl. Surf. Sci.* **2012**, 258 (16), 6116–6126.
- (60) Thomas, S.; Birbilis, N.; Venkatraman, M.; Cole, I. Corrosion of zinc as a function of pH. *Corrosion* **2012**, *68* (1), 015009.
- (61) Zheng, Y. F.; Gu, X. N.; Witte, F. Biodegradable metals. *Mater. Sci. Eng., R* **2014**, *77*, 1–34.
- (62) Yang, H.; Wang, C.; Liu, C.; Chen, H.; Wu, Y.; Han, J.; Jia, Z.; Lin, W.; Zhang, D.; Li, W.; Yuan, W.; Guo, H.; Li, H.; Yang, G.; Kong, D.; Zhu, D.; Takashima, K.; Ruan, L.; Nie, J.; Li, X.; Zheng, Y. Evolution of the degradation mechanism of pure zinc stent in the one-year study of rabbit abdominal aorta model. *Biomaterials* **2017**, *145*, 92–105.
- (63) Bourantas, C. V.; Onuma, Y.; Farooq, V.; Zhang, Y.; Garcia-Garcia, H. M.; Serruys, P. W. Bioresorbable scaffolds: current knowledge, potentialities and limitations experienced during their first clinical applications. *Int. J. Cardiol.* **2013**, *167* (1), 11–21.
- (64) Kumar, S.; Sankara Narayanan, T. S. N.; Ganesh Sundara Raman, S.; Seshadri, S. K. Evaluation of fretting corrosion behaviour of CP-Ti for orthopaedic implant applications. *Tribol. Int.* **2010**, *43* (7), 1245–1252.